

## Electronic structure and enhanced photoelectrocatalytic performance of $\text{Ru}_x\text{Zn}_{1-x}\text{O}/\text{Ti}$ electrodes

Yanqun SHAO<sup>a,b,\*</sup>, Keke FENG<sup>a</sup>, Jie GUO<sup>a</sup>, Rongrong ZHANG<sup>a</sup>, Sijiang HE<sup>a</sup>,  
Xinli WEI<sup>a</sup>, Yuting LIN<sup>a</sup>, Zhanghao YE<sup>a</sup>, Kongfa CHEN<sup>a</sup>

<sup>a</sup>College of Materials Science and Engineering, Fuzhou University, Fuzhou 350108, China

<sup>b</sup>College of Zhicheng, Fuzhou University, Fuzhou 350002, China

Received: January 4, 2021; Revised: April 16, 2021; Accepted: April 17, 2021

© The Author(s) 2021.

**Abstract:** Modification is one of the most important and effective methods to improve the photoelectrocatalytic (PEC) performance of ZnO. In this paper, the  $\text{Ru}_x\text{Zn}_{1-x}\text{O}/\text{Ti}$  electrodes were prepared by thermal decomposition method and the effect of Ru content on those electrodes' electronic structure was analyzed through the first-principles calculation. Various tests were also performed to observe the microstructures and PEC performance. The results showed that as the  $\text{Ru}^{4+}$  transferred into ZnO lattice and replaced a number of  $\text{Zn}^{2+}$ , the conduction band of ZnO moved downward and the valence band went upward. The number of photogenerated electron–hole pairs increased as the impurity levels appeared in the band gap. In addition, ZnO nanorods exhibited a smaller grain size and a rougher surface under the effect of Ru. Meanwhile, the  $\text{RuO}_2$  nanoparticles on the surface of ZnO nanorods acted as the electron-transfer channel, helping electrons transfer to the counter electrode and delaying the recombination of the electron–hole pairs. Specifically, the  $\text{Ru}_x\text{Zn}_{1-x}\text{O}/\text{Ti}$  electrodes with 9.375 mol% Ru exhibited the best PEC performance with a rhodamine B (RhB) removal rate of 97%, much higher than the combination of electrocatalysis (EC, 12%) and photocatalysis (PC, 50%), confirming the synergy of photoelectrocatalysis.

**Keywords:**  $\text{Ru}_x\text{Zn}_{1-x}\text{O}/\text{Ti}$  electrode; first-principles calculation; electric collector; photoelectric synergistic catalysis

### 1 Introduction

It was estimated that 15% of untreated organic dyes widely used in various fields have been discharged into water directly [1–4]. Those dyes could exist in the ecosystem stably, devastate its self-degradation ability, and make people suffer higher risk of intoxication, mutation, and cancerization. Therefore, how to cost-

effectively degrade organic dyes has become a hot topic [5–9]. One of the most widely studied methods would be the semiconductor material-based photocatalysis (PC) technology. And ZnO, an atoxic direct band gap semiconductor with a wide band gap of 3.37 eV and an exciton binding energy of 60 mV, has been considered as one of the most ideal materials for wastewater treatment due to its excellent PC activity, great physical and chemical stability as well as high cost efficiency [10–13]. It has been reported that compared with  $\text{TiO}_2$ , ZnO exhibited higher PC efficiency in terms

\* Corresponding author.

E-mail: yqshao1989@163.com

of the degradation of several organic contaminants in both acidic and basic medium [14–16]. However, the high recombination rate of photogenerated electron–hole pairs and oversized band gap have significantly limited its application. Hence, how to reduce the recombination rate and enlarge the light-absorption area have received much attention [17–20].

In recent years, an external bias potential placed between the anode and cathode has proven an effective method to promote the electron–hole separation rate. Under its effect, the fore-mentioned recombination rate was reduced, and more electrons and holes were allowed to participate in the reaction of oxidative cracking of organic dye as the photogenerated electrons were forced to move to the counter electrode through an external circuit, while the holes remained in the valence band thanks to the external electric field. In addition, Ma *et al.* [17] designed a dual-cocatalyst for spatial separation, of which Co–Pi as the outmost hole-transfer layer and Pt as the bottom electron collector and transport layer, and thereby photogenerated electron–hole pairs were separated effectively and twice higher current density was obtained. However, neither the external bias potential nor the electron collector could increase the yield of photogenerated electron–hole pairs, the light-absorption range was still relatively narrow. An efficient way to solve that problem was doping metal or non-metal elements into materials and changing their electronic structure and band gap [21–25]. Ashebir *et al.* [26] reported that both Mn- and Ag-doped ZnO nanoparticles showed a decreased band gap and higher PC performance relative to pure ZnO. According to Qiu *et al.* [27] who studied the effect of N-doping on the PC performance of ZnO, the forbidden band width decreased significantly and the PC activity was enhanced after the N 2p impurity energy level appeared. Doping could also change the microstructure of the material [24,28,29]. Etacheri *et al.* [30] revealed that Mg-doped ZnO exhibited a significant *c*-axis compression and decreased grain size, and its specific surface area was twice as large as that of pure ZnO.

In general, the bias potential and electron collector could reduce the recombination rate of photogenerated electron–hole pairs effectively, and doping method could expand the light-absorption area and change the material's microstructure [31]. Given the fact that noble metal oxide RuO<sub>2</sub> is an excellent electrocatalyst with high conductivity [32–35], the atomic radius

disparity between Ru<sup>4+</sup> and Zn<sup>2+</sup> is smaller than 7% making it possible to prepared Ru-doped ZnO, and the minute difference in electronegativity between the two atoms helps form solid solutions with greater solubility [36,37]. We finally chose Ru to modify ZnO and analyzed its impact on the electronic structure and the photoelectrocatalysis (PEC) performance of composite-oxide electrodes.

## 2 Experimental and calculation methods

### 2.1 Preparation of Ru<sub>x</sub>Zn<sub>1-x</sub>O/Ti electrodes

#### 2.1.1 Pretreatment of the Ti plates

In order to strengthen the bonding force between the substrate and the coatings, enlarge the surface area, and extend the service life of the electrodes, the sandblasted 20 mm×20 mm×1.5 mm TA2 titanium plate was degreased, etched in 10 wt% H<sub>2</sub>SO<sub>4</sub> for 2 h, and then cleaned with deionized water and preserved in absolute alcohol for further use.

#### 2.1.2 Preparation of Ru<sub>x</sub>Zn<sub>1-x</sub>O/Ti electrodes

The precursors RuCl<sub>3</sub>·*x*H<sub>2</sub>O (containing 37% Ru by mass) and ZnCl<sub>2</sub> were used to prepare the mixed solutions with Ru contents of 0, 3.125, 6.25, 9.375, and 12.5 mol%, which were stirred evenly by ultrasonic vibration. Then an appropriate amount of the mixed solution (3 μL·cm<sup>-2</sup>) was brushed on the Ti plates, which were cured under an infrared lamp at 100 °C for 10 min, and pre-oxidized in a muffle furnace at 500 °C for another 10 min, followed by air cooling. After repeating those steps for six times, the samples were annealed at 500 °C for 60 min, and then cooled in the air. The Ru<sub>x</sub>Zn<sub>1-x</sub>O/Ti electrodes with different Ru contents were prepared.

### 2.2 Characterization techniques

The microstructures of the Ru<sub>x</sub>Zn<sub>1-x</sub>O/Ti electrodes were observed by a scanning electron microscope (SEM, Supra 55, Carl Zeiss, Oberkochen, Germany) and the transmission electron microscope tests (TEM, TECNAI G2 F20, FEI, USA). The phase structures of the coatings were studied by X-ray diffractometer test (XRD, Ultima III, Rigaku, Tokyo, Japan) with Cu Kα radiation source and Ni filter, where the tube voltage and current were 36 kV and 30 mA respectively, and the angle range and scanning rate were 25°–60° and

2 (°)/min respectively. X-ray photoelectron spectroscopy (XPS) spectra were performed on the photoelectron spectroscopy system (Escalab 250, Thermo Scientific, USA), and the elemental peak fitting was performed via the Avantage software. The UV–Vis diffuse reflectance spectra (DRS) were tested through the UV2600 instrument with a wavelength range of 200–800 nm. Specific surface areas (SSA) were tested with the Micromeritics 3Flex specific surface analyzer, and the samples were degassed at 200 °C for 10 h.

### 2.3 First-principles calculations

According to the solid solution theory, both an ionic radius difference within 15% (Ru<sup>4+</sup> 0.62 Å vs. Zn<sup>2+</sup> 0.74 Å) and minute electronegativity disparity (Ru 2.20, Zn 1.65) are favorable factors, indicating the high possibility of forming Ru<sub>x</sub>Zn<sub>1-x</sub>O solid solution. Given that the ideal ZnO possesses a hexagonal wurtzite structure with a space group of *P63/mc*, a 2×2×2 supercell structure model with 64 atoms was constructed, in which a small number of Zn and Ru atoms exchanged places, as shown in Fig. 1. In this study, VASP software was adopted to calculate the electronic structure of the Ru-doped ZnO crystal based on the plane-wave density functional theory (DFT), where the *k*-point meshes of the Brillouin zone were obtained via 9×9×5 Monkhorst–Pack grid and the plane wave cut-off energy was 520 eV.

### 2.4 Electrochemical measurements

Electrochemical tests were performed with a three-electrode system via the Metrohm AUTOLAB electrochemical workstation (AUT84638, PGSTAT302N). 0.1 M Na<sub>2</sub>SO<sub>4</sub> solution was used as the electrolyte. The prepared Ru<sub>x</sub>Zn<sub>1-x</sub>O/Ti with different Ru contents was as working electrodes. The saturated calomel electrode (SCE) was as a reference electrode, and the large-area titanium plate was as a counter electrode. The amplitude for electrochemical impedance spectroscopy EIS (test) was

10 mV and the frequency range was 0.05–10<sup>5</sup> Hz. The linear sweep voltammetric (LSV) tests were performed with a potential range of 0–2.5 V and a scanning rate of 10 mV·s<sup>-1</sup>.

### 2.5 Photoelectrochemical measurement

The PEC performance of the Ru<sub>x</sub>Zn<sub>1-x</sub>O/Ti electrodes was evaluated by the degradation rate of RhB, methyl orange (MO), and methylene blue (MB). The experiment was also done with the above three-electrode set. The electrolyte in a 500 mL cylindrical quartz beaker was the mixed solution of 0.1 M Na<sub>2</sub>SO<sub>4</sub> and 20 mg·L<sup>-1</sup> RhB, 0.1 M Na<sub>2</sub>SO<sub>4</sub> and 20 mg·L<sup>-1</sup> MO, or 0.1 M Na<sub>2</sub>SO<sub>4</sub> and 20 mg·L<sup>-1</sup> MB, respectively. A 100 W ultraviolet mercury lamp (386 nm) was placed directly opposite to the working electrode with a surface area of 4 cm<sup>2</sup>, and the light intensity (15 mW·cm<sup>-2</sup>) was monitored via a light intensity photometer (UV-M10-P/S, ORC, Japan). The solution was continuously stirred, and the potential was 2.5 V. The removal rate of RhB during each degradation period was evaluated via a Cary 50 UV–Vis spectrophotometer (Varian, USA) and the total organic carbon (TOC) tests were carried out through Shimadzu TOC-L ASI-L (Shimadzu, Japan).

## 3 Results and discussion

### 3.1 Microstructure morphology analysis

As we seen from the SEM images of the Ru<sub>x</sub>Zn<sub>1-x</sub>O/Ti electrodes with different Ru contents shown in Fig. 2, the coating surface exhibited both large and small typical hexagonal prism ZnO grains [18,38]. According to Fig. 2(a), ZnO nanorods on the surface of pure ZnO coatings arranged orderly, possessing a relatively larger crystal grain diameter of 0.1–1 μm. However, as Ru content increased, ZnO nanorods tended to grow disorderly and the diameter gradually decreased with a

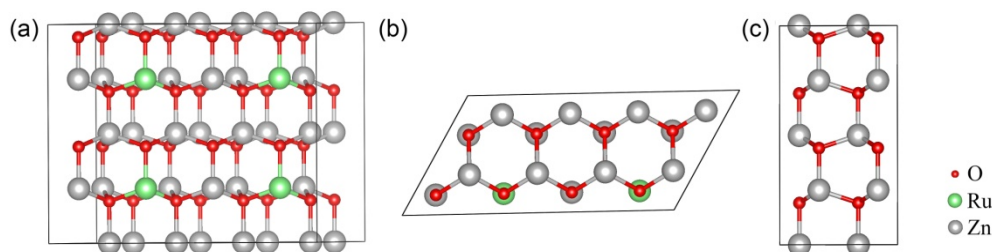


**Fig. 1** Ru-doped ZnO with hexagonal wurtzite crystal structure: (a) front view, (b) top view, and (c) left view.

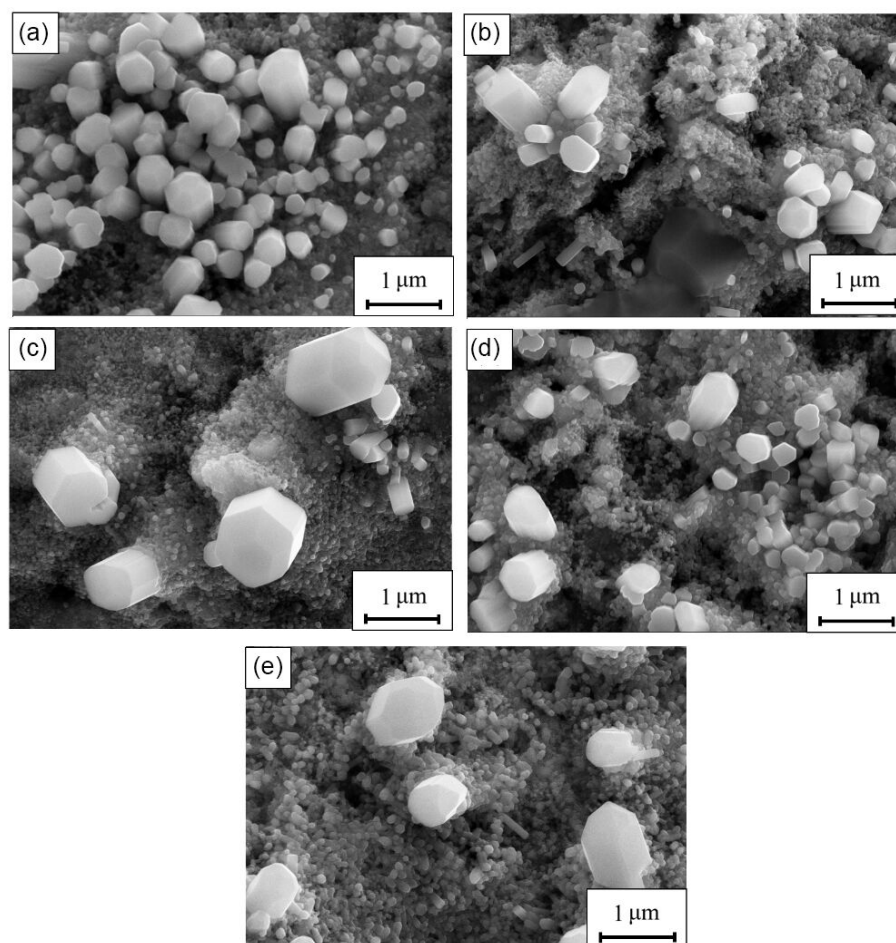


**Fig. 2** SEM images of  $\text{Ru}_x\text{Zn}_{1-x}\text{O}/\text{Ti}$  electrodes: (a) 0 mol%, (b) 3.125 mol%, (c) 6.25 mol%, (d) 9.375 mol%, and (e) 12.5 mol%.

few exceptions, i.e., adding Ru could reduce the grain size of ZnO, increase the irregularity degree of coatings, and thus enlarge the specific surface area.

Phase analysis of the  $\text{Ru}_x\text{Zn}_{1-x}\text{O}/\text{Ti}$  electrodes was carried out through the XRD tests. Pure ZnO electrodes only exhibited the diffraction peak of hexagonal wurtzite phase ZnO (space group:  $P63/mc$ , JCPDS 36-1451) as displayed in Fig. 3(a). Compared with pure ZnO,  $\text{Ru}_x\text{Zn}_{1-x}\text{O}/\text{Ti}$  electrode doped with Ru not only exhibited the diffraction peak of ZnO, but also the rutile phase  $\text{RuO}_2$  (space group:  $P42/mnm$ , JCPDS 18-1139) and tetragonal phase metal Ru (JCPDS 06-0663). In addition, the higher the Ru content, the more intensive the diffraction peaks of  $\text{RuO}_2$  and metallic Ru, while the intensity of ZnO diffraction peaks gradually decreased, suggesting that there might be more  $\text{RuO}_2$  particles covered on the surface of ZnO. The relatively sharper peak of ZnO indicated a higher degree of crystallization. The grain size of ZnO ( $D$ ) was calculated by the following Scherrer equation (applied to the (101) crystal plane) [39]:

$$D = \frac{k\lambda}{\beta \cos \theta} \quad (1)$$

where  $k$  is the Scherrer constant (0.89),  $\lambda$  is the X-ray wavelength of Cu  $K\alpha$  (0.154 nm),  $\beta$  is the full width at half maximum (FWHM) of the (101) crystal plane diffraction peak of ZnO, and  $\theta$  is the diffraction angle. According to the results shown in Table 1, the grain size of ZnO decreased from 33 to 26 nm with the increase of Ru content, coinciding with the SEM analysis [30,40–42]. As shown in Fig. 3(b), the  $2\theta$  angles of  $31.769^\circ$ ,  $34.421^\circ$ , and  $36.252^\circ$  corresponded to the (100), (002), and (101) crystal planes of hexagonal wurtzite phase ZnO, respectively. Compared with the pure ZnO electrodes, the  $2\theta$  of the three diffraction peaks of Ru-doped ones shifted to higher angles. The higher the Ru content, the larger the deviation degree, indicating that  $\text{Ru}_x\text{Zn}_{1-x}\text{O}$  solid solution could be formed after a number of  $\text{Zn}^{2+}$  in the ZnO lattice were replaced by  $\text{Ru}^{4+}$  with smaller radius. [41,43,44].

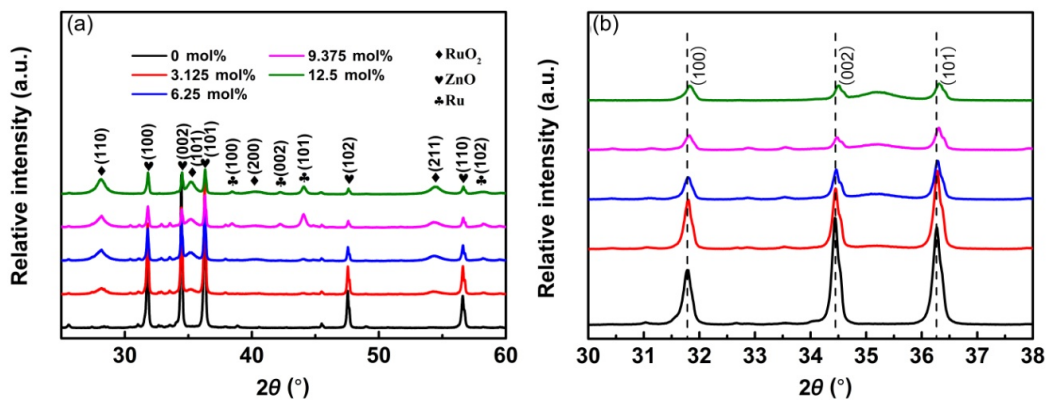


Fig. 3 XRD patterns of  $Ru_xZn_{1-x}O/Ti$  electrodes: (a)  $2\theta$  within  $25^\circ$ – $60^\circ$ ; (b) the enlarged view of  $2\theta$  within  $30^\circ$ – $38^\circ$ .

Table 1 Grain size of  $Ru_xZn_{1-x}O/Ti$  coatings

Content of $Ru^{4+}$ (mol%)	0	3.125	6.25	9.375	12.5
Grain size (nm)	33	30	29	28	26

Table 2 SSA of  $Ru_xZn_{1-x}O/Ti$  coatings

Content of $Ru^{4+}$ (mol%)	0	3.125	6.25	9.375	12.5
SSA ( $m^2 \cdot g^{-1}$ )	1.536	1.881	2.909	4.077	7.422

According to the results listed in Table 2, the specific surface area (SSA) of the  $Ru_xZn_{1-x}O/Ti$  electrodes increased gradually as the Ru content rose as adding Ru could reduce the grain size of ZnO nanorods and increase the coatings' irregularity degree, which helped provide more active sites for PEC degradation.

The microstructures of the  $Ru_xZn_{1-x}O/Ti$  electrodes were analyzed by transmission electron microscopy (TEM). Figures 4(a) and 4(b) reveal that the wurtzite-type ZnO nanorods were piled up by the (001) planes, coinciding with its single-crystal characteristic [38]. The selected area electron diffraction (SAED) pattern shown in Fig. 4(c) further confirmed that the three

diffraction spots corresponded to the (101), (100), and (002) crystal planes of ZnO, respectively. According to Fig. 4(d), the  $RuO_2$  nanoparticles distributed on the ZnO nanorods' surface uniformly, and this structure facilitated the transfer of electrons and the separation of photo-generated electrons and holes. The lattice spacing of 0.248 and 0.317 nm displayed in Fig. 4(e), corresponded to the (101) crystal plane of ZnO (JCPDS 36-1451) and the (110) crystal plane of  $RuO_2$  (JCPDS 18-1139), respectively. Figure 4(f) exhibits the polycrystalline electron diffraction pattern of ZnO and  $RuO_2$ , where the two diffraction spots corresponded to the (101) crystal planes of ZnO and the (110) crystal plane of  $RuO_2$ , respectively, consistent with the XRD analysis.

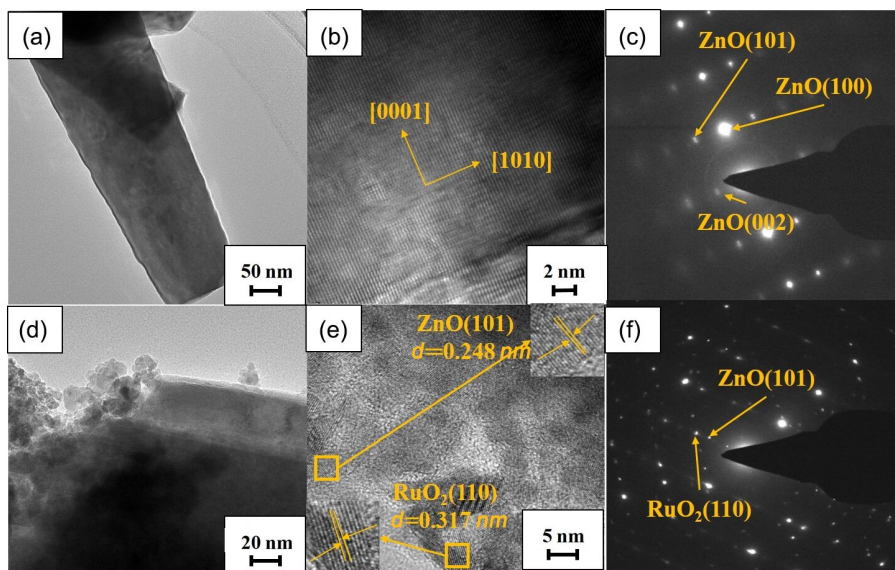


Fig. 4 TEM and SAED patterns of  $Ru_xZn_{1-x}O/Ti$  electrodes: (a–c) 0 mol% and (d–f) 9.375 mol%.

XPS analysis of  $\text{Ru}_x\text{Zn}_{1-x}\text{O}/\text{Ti}$  electrodes was carried out to identify the elements' composition and valence, and the results were adjusted with C 1s of 284.8 eV. According to Fig. 5(a), the full spectra of  $\text{Ru}_x\text{Zn}_{1-x}\text{O}/\text{Ti}$  electrodes have exhibited all the characteristic peaks of Ru 3d, Zn 2p, O 1s, and C 1s. The high-resolution narrow scan spectra of Ru 3d shown in Fig. 5(b) displayed a pair of narrow characteristic peaks, corresponding to the two spin-orbital components of Ru 3d<sub>5/2</sub> and Ru 3d<sub>3/2</sub>, respectively, which located at 280.48 and 284.98 eV with a spin separation energy of 4.5 eV when the Ru content was 9.375 mol% [45–47]. The Ru 3d characteristic peaks could be divided into five small peaks representing the form of different states of Ru, coinciding with the three existing forms of Ru (RA for Ru, RB for  $\text{RuO}_2$ , and RC for  $\text{RuO}_x/\text{Ru}$ , respectively, Fig. 5(b)) and C 1s. The peaks at 280.66 and 284.91 eV corresponded to  $\text{Ru}^{4+}$  in  $\text{RuO}_2$ , and obtained by heat treatment after the coatings were exposed to the surrounding environment. The one located at 280.45 eV was consistent with the zero valence of  $\text{Ru}^0$ , resulting from the disproportionation of  $\text{RuCl}_3$  or the insufficient oxygen supply during the heat treatment. The peak at 282.05 eV indicated the existence of  $\text{RuO}_x/\text{Ru}$  anoxic ruthenium, and the peak of C 1s appeared at 284.8 eV [47–49]. As shown in Table 3, compared with the electrodes with 9.375 mol% Ru, the Ru 3d characteristic peak of those containing

12.5 mol% Ru had a red-shift by 0.12 eV, as the  $\text{RuO}_2$  content decreased and the  $\text{RuO}_x/\text{Ru}$  content increased [50]. The high-resolution narrow scan spectra of Zn 2p in Fig. 5(c) exhibited two spin orbits of Zn 2p<sub>3/2</sub> and Zn 2p<sub>1/2</sub> with a spin separation energy of 23 eV. Pure ZnO electrodes displayed double peaks of Zn 2p<sub>3/2</sub> and Zn 2p<sub>1/2</sub> at 1021.41 and 1044.42 eV, respectively, corresponding to  $\text{Zn}^{2+}$  in ZnO [30,51]. Besides, those peaks had blue-shifted by 0.42 and 0.70 eV, when the Ru content was 9.375 mol% (1021.83 and 1044.85 eV) and 12.5 mol% (1022.11 and 1045.13 eV), respectively, due to the replacement between  $\text{Zn}^{2+}$  and  $\text{Ru}^{4+}$ . After the formation of Zn–O–Ru bond, the electron density around Zn atoms reduced as the electronegativity of Ru (2.20) was greater than that of Zn (1.65). Accordingly, the binding energy between the nucleus and extranuclear electrons of Zn atoms was strengthened, while that of Ru atoms was weakened, which was also one reason for the red shift of Ru 3d characteristic peak [30,52,53]. The high-resolution narrow scan spectra of O 1s are shown in Fig. 5(d), where the O 1s characteristic peaks of pure ZnO electrode could be divided into two. One was at 531.70 eV resulted from the adsorbed  $\text{O}_2$  or  $\text{OH}^-$  ions, while the other at 530.02 eV corresponded to  $\text{O}^{2-}$  in ZnO. It is noted that besides the aforementioned peaks, the electrodes containing Ru exhibited another O 1s characteristic peak at 529.40 eV, which was coincided with  $\text{O}^{2-}$  in  $\text{RuO}_2$ .

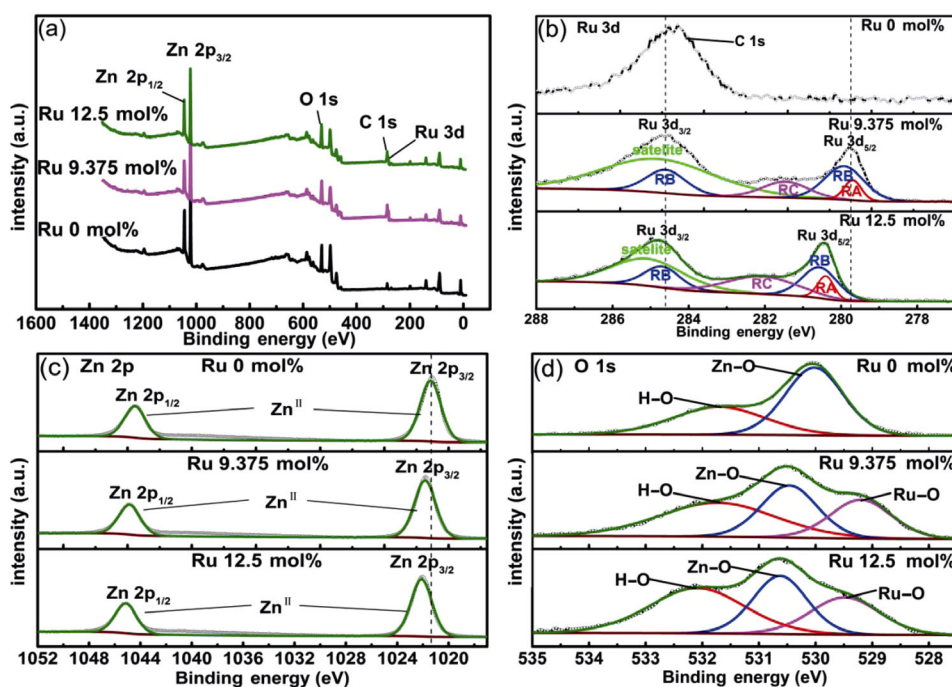


Fig. 5 XPS spectra of  $\text{Ru}_x\text{Zn}_{1-x}\text{O}/\text{Ti}$  coatings: (a) full spectra, (b) Ru 3d, (c) Zn 2p, and (d) O 1s.

**Table 3 Peak position and corresponding peak area ratio of XPS spectra of high-resolution Ru 3d and Zn 2p**

Composition (at%)	Orbital/spin	Peak position (eV)	Ratio of the integral area of the peak (%)	
			Ru 9.375 mol%	Ru 12.5 mol%
Ru	3d <sub>5/2</sub>	280.2±0.2	0.90	1.36
RuO <sub>x</sub> /Ru	3d <sub>5/2</sub>	281.9±0.2	1.88	5.64
RuO <sub>2</sub>	3d <sub>5/2</sub>	280.9±0.2	5.73	4.72
ZnO	2P <sub>3/2</sub>	1021.8±0.2	91.49	88.28

**3. 2 Band structure and density of state analysis**

The effect of Ru content on the electronic structure of Ru<sub>x</sub>Zn<sub>1-x</sub>O solid solution was analyzed by the first-principles calculation. The band and crystal structure characteristics were also explained in detail. According to the data listed in Table 4, the calculated results of this study were very close with other studies. The lattice parameters *a*, *c*, and unit cell volume (*V*<sub>0</sub>) of the solid solution, all decreased with the increase of Ru content, as the ionic radius of Ru (0.69 Å) was smaller than that of Zn (0.74 Å) [36,54]. The band structure and density of state (DOS) of Ru<sub>x</sub>Zn<sub>1-x</sub>O solid solution are shown in Fig. 6. Typically, the Fermi level is close to the central portion of the forbidden band [55]. As shown in Fig. 6(a), the minimum calculated energy gap (*E*<sub>g</sub>) of pure ZnO samples was about 1.78 eV, though smaller than the experimental value (3.37 eV), the result was still competitive with previous studies by Hernández *et al.* [56] (1.87 eV) and Bendavid and Carter [54] (1.90 eV). A possible reason was that the DFT theory did not take strong Coulomb correlation and interaction between electrons into consideration, leading to an underestimated band gap value. As shown in Figs. 6(a)–6(e), after adding Ru, the conduction band of ZnO moved down, the valence band moved up, and the impurity level appeared and narrowed the band gap. The higher the Ru content, the narrower the band

gap (1.44 eV for 3.125 mol%, 0.72 eV for 6.25 mol%, 0.39 eV for 9.375 mol%, and 0.24 eV for 12.5 mol%, respectively). In other words, the addition of Ru had a significant effect on the band structure of ZnO, reducing the electron-transfer energy barrier. According to the DOS of the Ru<sub>x</sub>Zn<sub>1-x</sub>O electrodes shown in Figs. 6(f)–6(j), pure ZnO samples exhibited peaks in four areas: Peaks ≈ -19 eV were mainly caused by the O 2s orbit, those appeared within the range of -9.5 to -7.5 eV and -6.5 to -1.5 eV were resulted from the hybridization of O 2p and Zn 3d orbits, and peaks located at the conduction band of about 8 eV were mainly formed by Zn 4s and O 2p. A significant difference in the electronic structure between Ru-doped and pure ZnO samples was that an impurity level appeared in the forbidden bands and narrowed the band gap, due to the electronic states of Ru 4d. As the Ru content increased, more electron energy levels appeared near the Fermi level, the electrons became more active, and the conductivity was enhanced accordingly. However, with the band gap narrowing down, the recombination rate of photogenerated electron-hole pairs also increased.

The UV-DRS tests were performed to observe the forbidden band width of the Ru<sub>x</sub>Zn<sub>1-x</sub>O/Ti coatings and the values were calculated through the following Tauc-plot method [59]:

$$\alpha hv = A(hv - E_g)^{1/n} \tag{2}$$

where *α* is the absorbance index; *h* is the Planck constant; *ν* is the frequency constant. *A* represents the slope of the Tauc edge; *n* equals to 2, determined by the semiconductor type; and *E*<sub>g</sub> is the band gap, reflected by the intersection point of the linear part of the curve of (*αhv*)<sup>2</sup> and the *hν* axis. According to the results shown in Fig. 7, the band gap (3.12 eV) of pure ZnO was slightly smaller than the theoretical value (3.37 eV) because of the lack of oxygen [60]. Besides,

**Table 4 Comparison of calculated and experimental values of parameters (*a* and *c*) and lattice volume (*V*<sub>0</sub>) of Ru<sub>x</sub>Zn<sub>1-x</sub>O/Ti solid solution**

Composition	<i>a</i> (Å)	<i>c</i> (Å)	<i>α, β, γ</i> (°)	<i>V</i> <sub>0</sub> (Å <sup>3</sup> )	Ref.
ZnO	3.250	5.207	90, 90, 120	47.600	JCPDS 36-1451
ZnO	3.250	5.232	90, 90, 120	—	[57]
ZnO	3.252	5.222	90, 90, 120	—	[58]
0 mol% Ru	3.249	5.145	90, 90, 120	46.900	This work
3.125 mol% Ru	3.242	5.136	89.968, 90, 120.209	46.348	This work
6.25 mol% Ru	3.232	5.098	89.995, 90, 120.017	46.263	This work
9.375 mol% Ru	3.226	5.077	89.018, 90.888, 121.171	46.200	This work
12.5 mol% Ru	3.224	5.055	88.392, 91.499, 121.249	46.168	This work

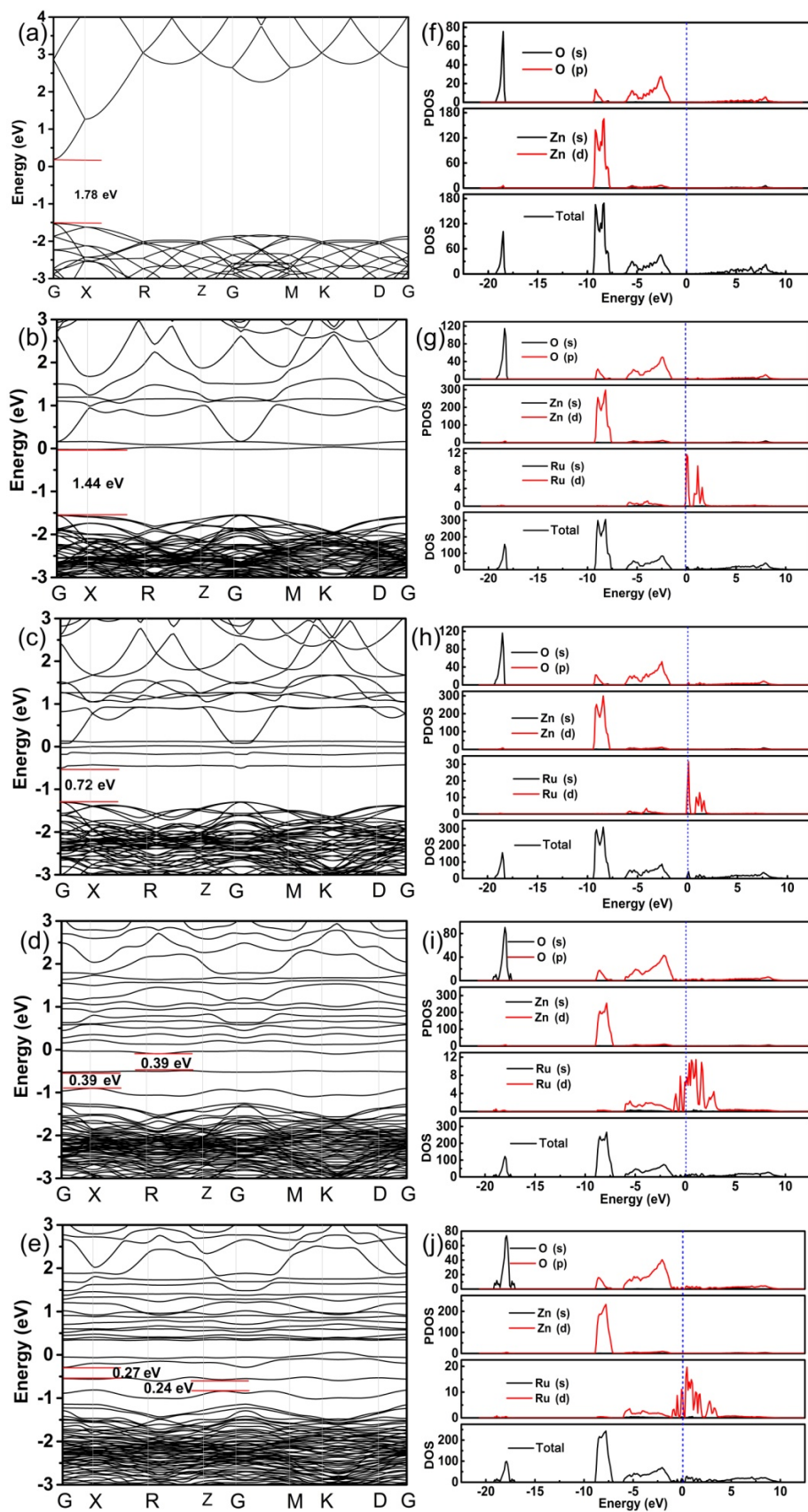


**Fig. 6** Band structures and densities of state of the  $\text{Ru}_x\text{Zn}_{1-x}\text{O}$  solid solution: (a, f) 0 mol%, (b, g) 3.125 mol%, (c, h) 6.25 mol%, (d, i) 9.375 mol%, and (e, j) 12.5 mol%.

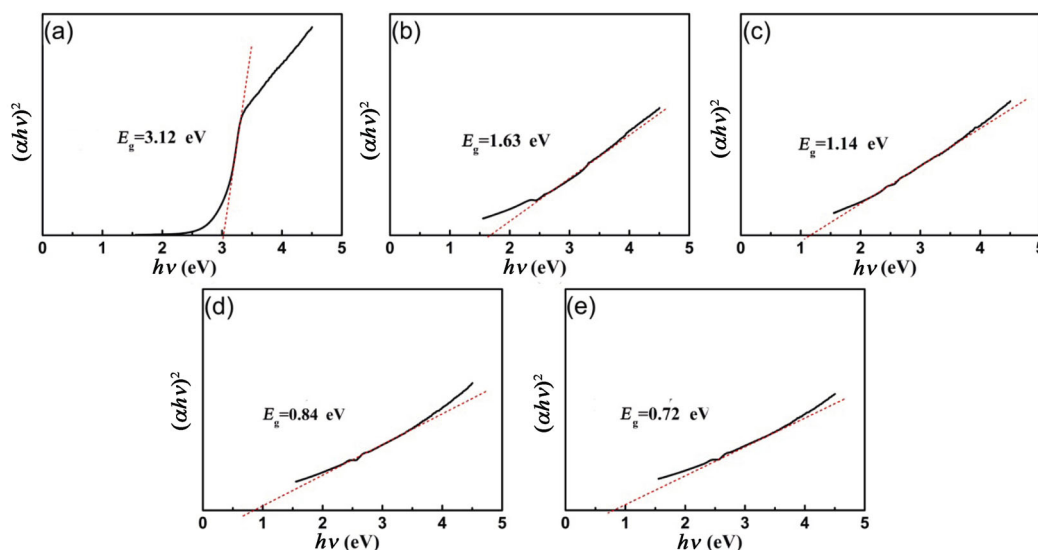


**Fig. 7** UV-DRS patterns of the  $Ru_xZn_{1-x}O/Ti$  coatings: (a) 0 mol%, (b) 3.125 mol%, (c) 6.25 mol%, (d) 9.375 mol%, and (e) 12.5 mol%.

the band gap decreased with the increase of Ru content, coinciding with the theoretical calculation results.

### 3.3 Electrochemical measurements

As shown in Fig. 8, the LSV test of the  $Ru_xZn_{1-x}O/Ti$  electrodes without and with UV irradiation was performed at a scanning rate of  $10\text{ mV}\cdot\text{s}^{-1}$ . It can be seen that when the potential exceeded 1.6 V, the current densities increased rapidly due to the electrolyzed water. With the rise of Ru content, the current densities increased first, then decreased, with or without UV irradiation, and reached the maximum when the content was 9.375 mol%. This was partly because pure ZnO coatings had a relatively larger band gap and poorer conductivity, leading to a lower current density when voltage remained the same. With the addition of Ru, coatings' band gap decreased and the conductivity was improved, resulting in an increased number of active photo-generated electron-hole pairs which enhanced current density. However, with a Ru content of 12.5 mol%,

excessive  $RuO_2$  particles would pile up on ZnO nanorods' surface, narrowing its effective light-sensitive area. Besides, the narrowed band gap also resulted in an increasing electron-hole recombination rate. As we can see from Figs. 8(a) and 8(b), samples under UV irradiation exhibited stronger current densities due to the generation of photocurrent.

Figure 9(a) shows the Nyquist plots of the  $Ru_xZn_{1-x}O/Ti$  electrodes, and the enlarged view of its high frequency region is displayed in Fig. 9(c), where the points and lines referred to the experimental and fitted data, respectively. Figure 9(b) exhibits the equivalent circuit, in which  $L$  represents the inductive reactance of the electrochemical system,  $R_s$  refers to the intersection of the high frequency region and the real axis, reflecting the sum of the solution resistance and the coatings' internal resistance,  $R_f$  and  $R_{ct}$  indicate the coating-substrate or coating-electrolyte resistance and the Faraday transfer resistance, respectively, and  $Z_w$  is the Warburg impedance, representing the ionic diffusion

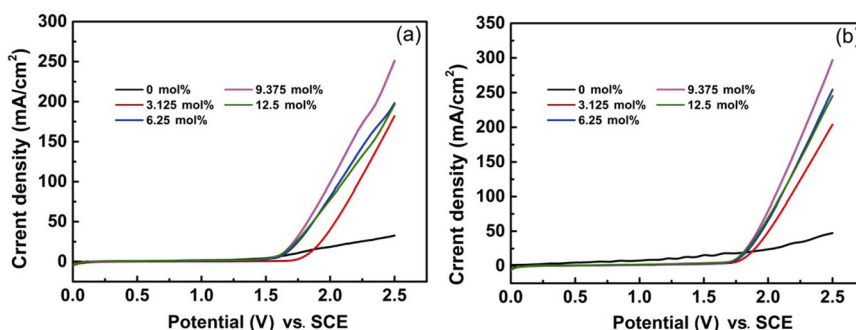


**Fig. 8** LSV curves of the  $Ru_xZn_{1-x}O/Ti$  electrodes: (a) without and (b) with UV irradiation.

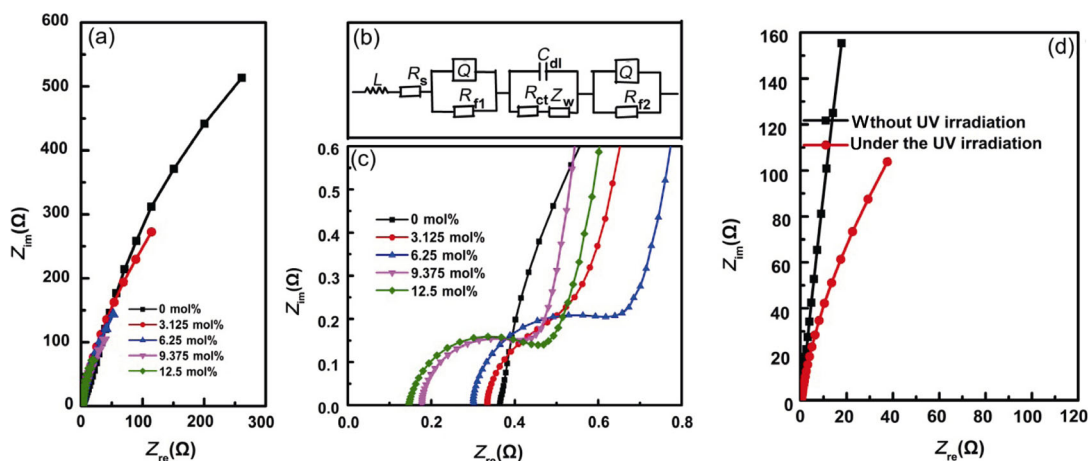


**Fig. 9** (a) Nyquist plots of the  $\text{Ru}_x\text{Zn}_{1-x}\text{O}/\text{Ti}$  electrodes; (b) electrical equivalent circuit for the fitting of the impedance spectra; (c) enlarged view of the high frequency region of the Nyquist plots; (d) Nyquist plots with and without UV irradiation.

process taking place on the interface between the electrodes and electrolyte.  $Q$  reflects a constant phase angle element, and  $C_{dl}$  refers to the double-layer capacitance [61–63]. According to the results from Fig. 9(c),  $R_s$  decreased all the way as the Ru content increased, indicating a reduced internal resistance. The diameter of the semicircle curve in the high-frequency region reflected the charge-transfer resistance, which decreased first, then increased, and reached to the minimum when the Ru content was 9.375 mol%, suggesting the electrodes' highest separation rate and transfer efficiency. As shown in Fig. 9(d), compared with the impedance spectrum of electrodes without UV irradiation, those under the light exhibited a larger inclination degree at the low frequency region, indicating that the UV irradiation accelerated the ion-diffusion rate.

### 3.4 Photoelectrocatalytic degradation of RhB

As we can see from the UV–Vis absorption spectra and the removal rate of RhB during PEC degradation process exhibited in Figs. 10(a)–10(f), the strongest absorption peak of RhB located at 554 nm. The peaks' intensity decreased as the degradation time increased, and the one corresponding to the electrode with 9.375 mol% Ru disappeared first. According to Fig. 10(f), as the Ru content rose, the removal rate increased first, from 71% of the pure ZnO electrode (120 min), and then decreased after reaching to the maximum of 97% (electrode containing 9.375 mol% Ru), indicating that doping appropriate amount of Ru could significantly improve electrodes' degradation efficiency. The TOC test results shown in Fig. 10(g)

confirmed that the addition of Ru could improve the TOC removal rate effectively, which exhibited an inverted U-shaped curve and reached to the maximum of 68% when the Ru content was 9.375 mol%. This was partly because the shortage of wide forbidden band of pure ZnO coatings and related problems including relatively smaller light-sensitive area and lower yield of photogenerated carriers could be overcome by adding Ru. Meanwhile, the  $\text{RuO}_2$  particles growing on ZnO surface provided an efficient electron-transfer channel and reduced the recombination rate of photogenerated electron–hole pairs. And the coatings' surface became less smooth with the addition of Ru, providing more active sites. However, with a Ru content of 12.5 mol%, excessive  $\text{RuO}_2$  particles wrapped around ZnO surface, hindering the irradiation of ultraviolet light. Though the forbidden band width of ZnO decreased after adding Ru, undersized band gap could accelerate the recombination rate of photogenerated electron–hole pairs in turn. That explained why the electrodes containing 9.375 mol% Ru exhibited the highest degradation rate.

In order to further illustrate the effect of Ru content on the degradation rate, the degradation kinetic analysis was carried out under the direction of the following first-order kinetic equation [64]:

$$-\ln\left(\frac{C_0}{C}\right) = kt \quad (3)$$

where  $C_0$  is the initial concentration of the RhB solution ( $20 \text{ mg}\cdot\text{L}^{-1}$ ),  $C$  is the concentration of RhB for a given degradation time,  $k$  is the reaction rate constant ( $\text{min}^{-1}$ ), and  $t$  is the reaction time. As the Ru content rose,  $k$  value increased first, then decreased, and reached

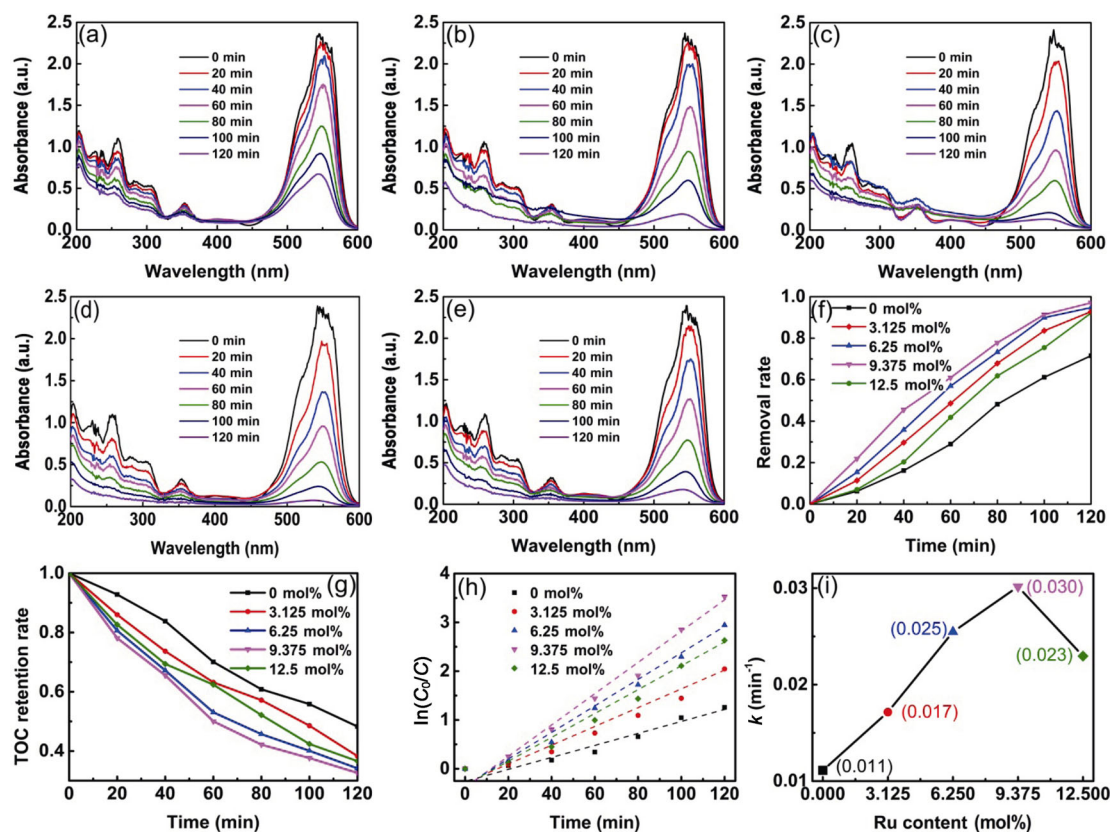


**Fig. 10** UV–Vis absorption spectra of  $Ru_xZn_{1-x}O/Ti$  electrodes under PEC degradation with different intervals: (a) 0 mol%, (b) 3.125 mol%, (c) 6.25 mol%, (d) 9.375 mol%, and (e) 12.5 mol%; (f) removal ratio of RhB; (g) TOC retention rate; (h) degradation kinetics; (i) reaction rate constant.

to the maximum of 0.03 when the content was 9.375 mol%, indicating the electrodes’ highest removal rate.

In order to further confirm the photoelectrocatalytic performance of  $Ru_xZn_{1-x}O/Ti$  electrodes, the degradation amount of RhB (2 h) was adopted to calculate the TON and TOF values, and the calculation equations are shown below [65]:

$$TON = C_{RhB}/C_{Cat} \tag{4}$$

$$TOF = TON/t \tag{5}$$

where  $C_{RhB}$  represents the concentration of the RhB involved in the reaction (mmol/L),  $C_{Cat}$  refers to the concentration of the catalyst in the solution (mmol/L), and  $t$  is the reaction time (h). The results are listed in Table 5. With the increase of Ru content, both the TON and TOF values increased first and then decreased, and reached the maximum when the Ru content was 9.375%. It is indicated that this electrode had the highest catalytic activity, which was consistent with the RhB catalytic degradation test. It is speculated that adding Ru could enlarge the number of photogenerated electrons produced by ZnO and help transfer electrons

**Table 5** TON and TOF values calculated with the degradation amount of RhB (2 h)

Content of $Ru^{4+}$ (mol%)	0	3.125	6.25	9.375	12.5
TON	0.21	0.27	0.28	0.29	0.27
TOF ( $h^{-1}$ )	0.11	0.13	0.14	0.15	0.13

more quickly, which effectively improved the catalytic activity of the electrodes and enhanced the photoelectrocatalytic degradation efficiency.

To make further explanation, the PC and electrocatalysis (EC) degradation tests of  $Ru_xZn_{1-x}O/Ti$  electrodes containing 9.375 mol% Ru were also performed, and the results are shown in Fig. 11. With a degradation time of 120 min, the removal rates of EC, PC, and PEC were 12%, 50%, and 97%, respectively. The much higher PEC efficiency confirmed the synergy effect of EC and PC degradation. According to the test results displayed in Fig. 11(g), after 120 min of degradation, the TOC removal rates for PEC, PC, and EC were 68%, 44%, and 10%, respectively. Compared with EC, the photogenerated electron–hole pairs generated during the PEC process, and the holes could decompose RhB

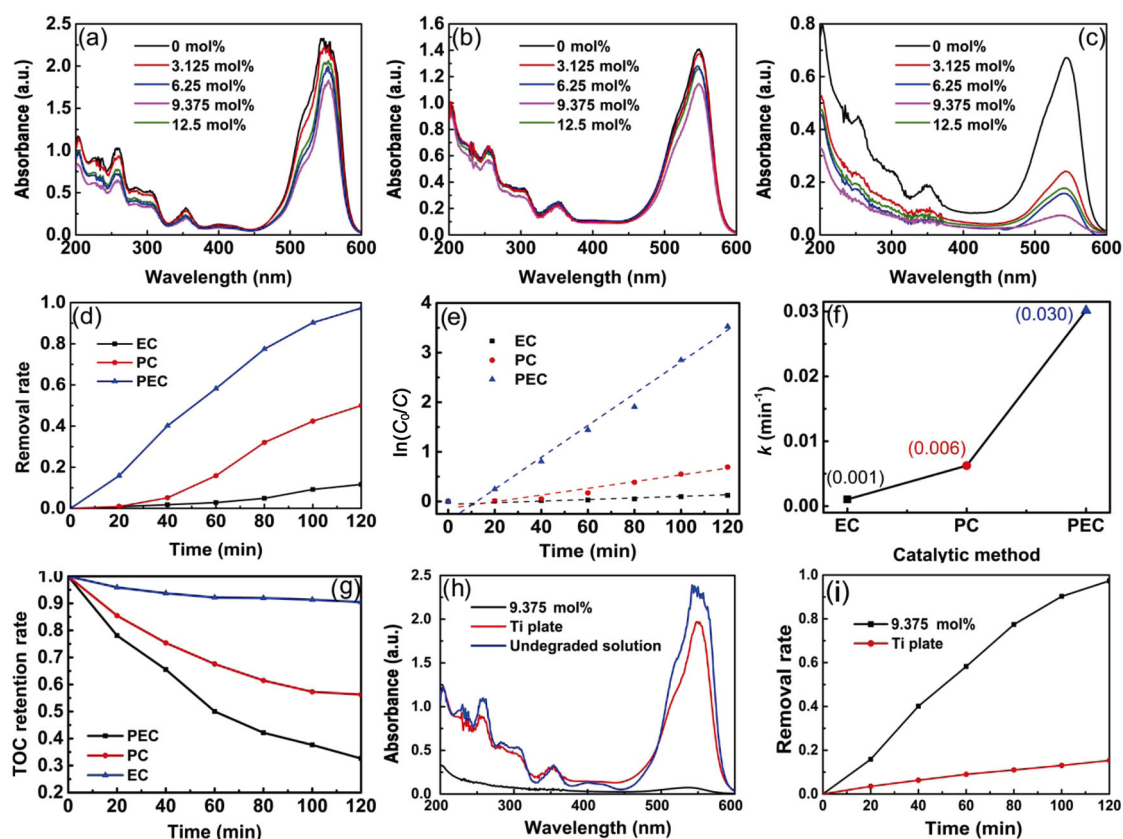


**Fig. 11** UV-Vis absorption spectra of  $\text{Ru}_x\text{Zn}_{1-x}\text{O}/\text{Ti}$  electrodes with 9.375 mol% Ru at different catalytic methods: (a) EC, (b) PC, (c) PEC, (d) removal rate; (e) degradation kinetics; (f) reaction rate constant; (g) TOC retention rate; (h) UV-Vis absorption spectra after 120-min PEC degradation by Ti and  $\text{Ru}_x\text{Zn}_{1-x}\text{O}/\text{Ti}$  electrodes with 9.375 mol% Ru; (i) PEC removal rate.

directly, and oxidize hydroxide ions on the electrodes' surface into hydroxyl radicals, which would oxidize RhB in turn. Compared with PC, PEC was provided with an external power source, and the  $\text{RuO}_2$  particles on the ZnO surface acting as an electro-transfer channel, offered more active sites for electrocatalysis and helped separate the photogenerated electron-hole pairs. In addition, a bias potential of 2.5 V facilitated the oxygen evolution reaction, providing the oxygen needed to oxidize RhB. It can be seen from Figs. 11(e) and 11(f) that the regression curve basically accorded with first-order kinetics, and the rate constant of PEC ( $0.030 \text{ min}^{-1}$ ) was much larger than that of EC ( $0.001 \text{ min}^{-1}$ ) and PC ( $0.006 \text{ min}^{-1}$ ), confirming the synergy effect of PEC degradation again. As shown in Figs. 11(h) and 11(i), the PEC degradation rate of Ti plate was only 15.3% after 120 min, and therefore, its effect on the  $\text{Ru}_x\text{Zn}_{1-x}\text{O}/\text{Ti}$  electrodes' degradation rate could be ignored.

MO and MB were adopted to further identify the degradation ability of the  $\text{Ru}_x\text{Zn}_{1-x}\text{O}/\text{Ti}$  electrode containing 9.375 mol% Ru, and the experiment results

are shown in Fig. 12. As we can see, the electrodes only took 60 and 40 min to remove 96% of MO and 98% of MB, respectively. It is sure that the  $\text{Ru}_x\text{Zn}_{1-x}\text{O}/\text{Ti}$  electrodes have good PEC performance and can effectively remove a variety of organic substances. The degradation performance of the material prepared in this study was compared with those reported by other articles, which adopted the same preparation method or similar composition materials, shown in Table 6. We can see that the  $\text{Ru}_x\text{Zn}_{1-x}\text{O}/\text{Ti}$  electrodes could almost degrade the organics in a relatively shorter time, better than most of other materials containing ZnO. The main reason might be that doping Ru could increase the number of photogenerated electron-hole pairs and their separation rates at the same time.

### 3.5 Photoelectrocatalytic mechanism

A preliminary schematic diagram of the PEC degradation mechanism of  $\text{Ru}_x\text{Zn}_{1-x}\text{O}/\text{Ti}$  electrodes based on a systematic analysis is presented in Fig. 13. With the addition of Ru, a number of Zn atoms were replaced and the substitutional solid solution was formed

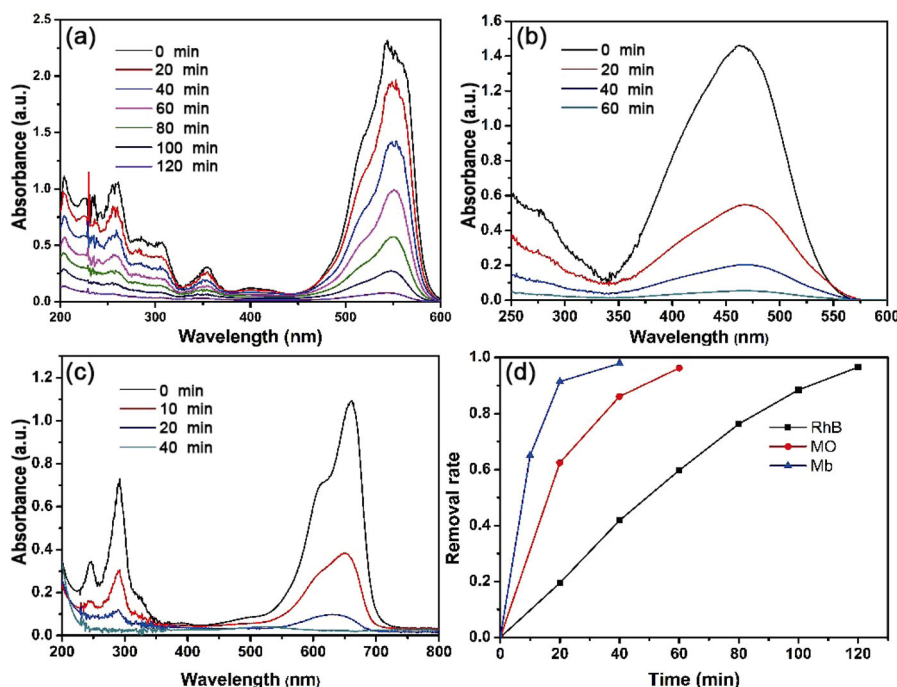


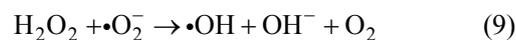
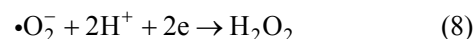
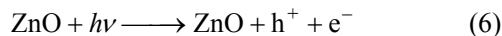
**Fig. 12** UV–Vis absorption spectra of  $Ru_xZn_{1-x}O/Ti$  electrodes containing 9.375 mol% Ru: (a) RhB, (b) MO, (c) MB, and (d) removal rate.

**Table 6** Contrastive analysis of degradation performance between materials prepared in this work and other studies

Reported material	Organics	Degradation time (min)	Removal rate	Ref.
$Ru_xZn_{1-x}O/Ti$	RhB	120	97%	This work
$Ru_xZn_{1-x}O/Ti$	MO	60	96%	This work
$Ru_xZn_{1-x}O/Ti$	Mb	40	98%	This work
Ag/ZnO	Phenol	180	100%	[64]
$Ir_xZn_{1-x}O/Ti$	RhB	80	99.4%	[66]
$Ti/Ru_xTi_{1-x}O$	MO	150	68%	[61]
Y/V/ZnO	RhB	180	89%	[39]
CdO/ZnO	4-nitrophenol	60	60%	[67]
Cu/GZnO	MO	80	89.1%	[68]

accordingly, which not only brought impurity levels to the forbidden band of ZnO, but also reduced the conduction band from E1 to E3, and increased the valence band from E2 to E4. That reduced the forbidden band width of ZnO and enlarged its light absorption range substantially, meaning that it could generate more photo-generated electron–hole pairs. In addition,  $RuO_2$  nanoparticles attaching on the surface of ZnO nanorods could provide effective electron transport channels and electrocatalytically active sites [69,70]. Under the effect of an external electric field, photogenerated electrons could be quickly transferred to the counter electrode and separate photogenerated

electron–hole pairs efficiently. Furthermore, those electrons could react with molecular oxygen and generate superoxide radicals, which then react with hydrogen ions to generate hydroxyl radicals in turn [71]. Meanwhile, holes could directly decompose organic dyes and oxidize hydroxide ions into hydroxyl radicals [72], which could degrade RhB into harmless compounds, such as  $H_2O$  and  $CO_2$  (the specific reaction process was shown in Eqs. (6)–(13)) [73,74]. The  $Ru_xZn_{1-x}O/Ti$  electrodes combined the advantages of ZnO (excellent photocatalytic ability) and  $RuO_2$  (good electron-transfer and electrocatalytic ability), which achieved a synergistic effect making the composite electrodes possess a degradation ability more powerful than the mere sum of photocatalysis and electrocatalysis.



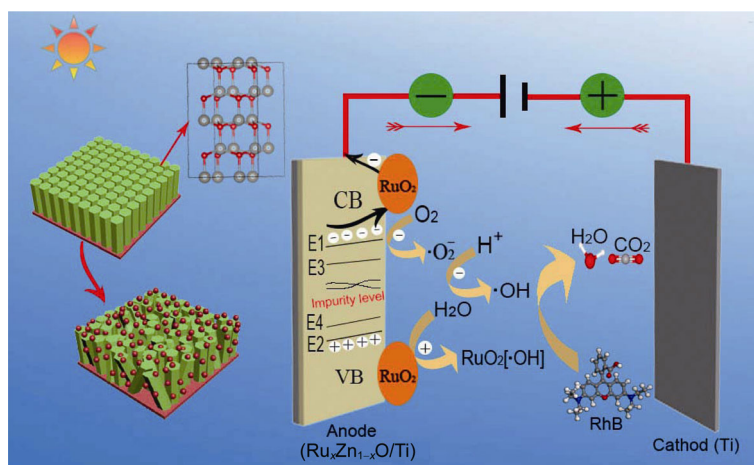


Fig. 13 Schematic microstructure model and PEC mechanism of  $\text{Ru}_x\text{Zn}_{1-x}\text{O}/\text{Ti}$  electrodes.

## 4 Conclusions

$\text{Ru}_x\text{Zn}_{1-x}\text{O}/\text{Ti}$  electrodes with excellent PEC performance were prepared through simple thermal decomposition method. It has been found that Ru-doped ZnO exhibited a smaller forbidden band width as a number of  $\text{Zn}^{2+}$  and  $\text{Ru}^{4+}$  exchanged places in ZnO lattice, and the amount of photogenerated carriers increased accordingly. The rest of Ru existed on the ZnO nanorods' surface in the form of  $\text{RuO}_2$  particles acting as an electron-transfer channel, together with the external bias, and it propelled photogenerated electrons to transfer to the counter electrode and reduced the recombination rate of electron–hole pairs. Meanwhile, with the addition of Ru, the grain size of ZnO nanorods decreased and the coatings' surface became less smooth, leading to larger specific surface area as well as more active sites. The accessory oxygen evolution reaction could also accelerate the oxidation of the dye. However, with excessive Ru content,  $\text{RuO}_2$  particles could wrap ZnO nanorods around and hinder the irradiation of ultraviolet light, reducing the PEC efficiency. Indeed, the band gap decreased with the addition of Ru, but undersized band gap could accelerate the recombination rate of photogenerated electron–hole pairs. That explained why the electrodes with 9.375 mol% rather than those containing 12.5 mol% Ru exhibited the best PEC performance.

## Acknowledgements

The work was supported by the National Natural Science Foundation of China (83418083) and the Natural Science Foundation of Fujian Province (2019J01230).

## References

- [1] Weber EJ, Adams RL. Chemical- and sediment-mediated reduction of the azo dye disperse blue 79. *Environ Sci Technol* 1995, **29**: 1163–1170.
- [2] Zhang FL, Zhao JC, Shen T, *et al.*  $\text{TiO}_2$ -assisted photodegradation of dye pollutants II. Adsorption and degradation kinetics of eosin in  $\text{TiO}_2$  dispersions under visible light irradiation. *Appl Catal B: Environ* 1998, **15**: 147–156.
- [3] Maleki A.  $\text{Fe}_3\text{O}_4/\text{SiO}_2$  nanoparticles: An efficient and magnetically recoverable nanocatalyst for the one-pot multicomponent synthesis of diazepines. *Tetrahedron* 2012, **68**: 7827–7833.
- [4] Maleki A. One-pot multicomponent synthesis of diazepine derivatives using terminal alkynes in the presence of silica-supported superparamagnetic iron oxide nanoparticles. *Tetrahedron Lett* 2013, **54**: 2055–2059.
- [5] Afzaal M, Malik MA, O'Brien P. Preparation of zinc containing materials. *New J Chem* 2007, **31**: 2029–2040.
- [6] Kamat PV. Meeting the clean energy demand: Nanostructure architectures for solar energy conversion. *J Phys Chem C* 2007, **111**: 2834–2860.
- [7] Roshan S A, Joseph C, Ittyachen MA. Growth and characterization of a new metal-organic crystal: Potassium thiourea bromide. *Mater Lett* 2001, **49**: 299–302.
- [8] Vayssieres L. Growth of arrayed nanorods and nanowires of ZnO from aqueous solutions. *Adv Mater* 2003, **15**: 464–466.
- [9] Maleki A. One-pot three-component synthesis of pyrido[2,1':2,3]imidazo[4,5-c]isoquinolines using  $\text{Fe}_3\text{O}_4@\text{SiO}_2\text{-OSO}_3\text{H}$  as an efficient heterogeneous nanocatalyst. *RSC Adv* 2014, **4**: 64169–64173.
- [10] Kumar SG, Rao KSRK. Zinc oxide based photocatalysis: Tailoring surface-bulk structure and related interfacial charge carrier dynamics for better environmental applications. *RSC Adv* 2015, **5**: 3306–3351.
- [11] Kim KJ, Kreider PB, Choi C, *et al.* Visible-light-sensitive

- Na-doped p-type flower-like ZnO photocatalysts synthesized via a continuous flow microreactor. *RSC Adv* 2013, **3**: 12702–12710.
- [12] Maleki A. Green oxidation protocol: Selective conversions of alcohols and alkenes to aldehydes, ketones and epoxides by using a new multiwall carbon nanotube-based hybrid nanocatalyst via ultrasound irradiation. *Ultrason Sonochem* 2018, **40**: 460–464.
- [13] Varzi Z, Maleki A. Design and preparation of ZnS–ZnFe<sub>2</sub>O<sub>4</sub>: A green and efficient hybrid nanocatalyst for the multicomponent synthesis of 2,4,5-triaryl-1H-imidazoles. *Appl Organomet Chem* 2019, **33**: e5008.
- [14] Lee JC, Park S, Park HJ, *et al.* Photocatalytic degradation of TOC from aqueous phenol solution using solution combusted ZnO nanopowders. *J Electroceramics* 2009, **22**: 110–113.
- [15] Khassin AA, Yurieva TM, Kaichev VV, *et al.* Metal-support interactions in cobalt–aluminum co-precipitated catalysts: XPS and CO adsorption studies. *J Mol Catal A: Chem* 2001, **175**: 189–204.
- [16] Maleki A, Varzi Z, Hassanzadeh-Afrouzi F. Preparation and characterization of an eco-friendly ZnFe<sub>2</sub>O<sub>4</sub>@alginic acid nanocomposite catalyst and its application in the synthesis of 2-amino-3-cyano-4H-pyran derivatives. *Polyhedron* 2019, **171**: 193–202.
- [17] Ma CH, Liu ZF, Cai QJ, *et al.* ZnO photoelectrode simultaneously modified with Cu<sub>2</sub>O and Co–Pi based on broader light absorption and efficiently photogenerated carrier separation. *Inorg Chem Front* 2018, **5**: 2571–2578.
- [18] Zhang SC, Liu ZF, Ruan MN, *et al.* Enhanced piezoelectric-effect-assisted photoelectrochemical performance in ZnO modified with dual cocatalysts. *Appl Catal B: Environ* 2020, **262**: 118279.
- [19] Maleki A, Hajizadeh Z, Sharifi V, *et al.* A green, porous and eco-friendly magnetic geopolymer adsorbent for heavy metals removal from aqueous solutions. *J Clean Prod* 2019, **215**: 1233–1245.
- [20] Maleki A, Mohammad M, Emdadi Z, *et al.* Adsorbent materials based on a geopolymer paste for dye removal from aqueous solutions. *Arab J Chem* 2020, **13**: 3017–3025.
- [21] Wang XQ, Zhou YN, Li R, *et al.* Removal of Hg<sup>0</sup> from a simulated flue gas by photocatalytic oxidation on Fe and Ce co-doped TiO<sub>2</sub> under low temperature. *Chem Eng J* 2019, **360**: 1530–1541.
- [22] Zhao SW, Zuo HF, Guo YR, *et al.* Carbon-doped ZnO aided by carboxymethyl cellulose: Fabrication, photoluminescence and photocatalytic applications. *J Alloys Compd* 2017, **695**: 1029–1037.
- [23] Zhao W, Zhong Q, Pan YX, *et al.* Systematic effects of S-doping on the activity of V<sub>2</sub>O<sub>5</sub>/TiO<sub>2</sub> catalyst for low-temperature NH<sub>3</sub>-SCR. *Chem Eng J* 2013, **228**: 815–823.
- [24] Kayani ZN, Anjum M, Riaz S, *et al.* Role of Mn in biological, optical, and magnetic properties ZnO nanoparticles. *Appl Phys A* 2020, **126**: 1–17.
- [25] Maleki A, Kari T. Novel leaking-free, green, double core/shell, palladium-loaded magnetic heterogeneous nanocatalyst for selective aerobic oxidation. *Catal Lett* 2018, **148**: 2929–2934.
- [26] Ashebir ME, Tesfamariam GM, Nigussie GY, *et al.* Structural, optical, and photocatalytic activities of Ag-doped and Mn-doped ZnO nanoparticles. *J Nanomater* 2018, **2018**: 1–9.
- [27] Qiu YF, Fan HB, Tan GP, *et al.* Effect of nitrogen doping on the photo-catalytic properties of nitrogen doped ZnO tetrapods. *Mater Lett* 2014, **131**: 64–66.
- [28] Ditta MA, Farrukh MA, Ali S, *et al.* X-ray peak profiling, optical parameters and catalytic properties of pure and CdS doped ZnO–NiO nanocomposites. *Russ J Appl Chem* 2017, **90**: 151–159.
- [29] Maleki A, Kari T, Aghaei M. Fe<sub>3</sub>O<sub>4</sub>@SiO<sub>2</sub>@TiO<sub>2</sub>–OSO<sub>3</sub>H: An efficient hierarchical nanocatalyst for the organic quinazolines syntheses. *J Porous Mater* 2017, **24**: 1481–1496.
- [30] Etacheri V, Roshan R, Kumar V. Mg-doped ZnO nanoparticles for efficient sunlight-driven photocatalysis. *ACS Appl Mater Interfaces* 2012, **4**: 2717–2725.
- [31] Soltaninejad V, Maleki A. A green, and eco-friendly bionanocomposite film (poly(vinyl alcohol)/TiO<sub>2</sub>/chitosan/chlorophyll) by photocatalytic ability, and antibacterial activity under visible-light irradiation. *J Photochem Photobiol A: Chem* 2021, **404**: 112906.
- [32] Han JS, An HJ, Kim TW, *et al.* Effect of structure-controlled ruthenium oxide by nanocasting in electrocatalytic oxygen and chlorine evolution reactions in acidic conditions. *Catalysts* 2019, **9**: 549.
- [33] Peng F, Zhou CM, Wang HJ, *et al.* The role of RuO<sub>2</sub> in the electrocatalytic oxidation of methanol for direct methanol fuel cell. *Catal Commun* 2009, **10**: 533–537.
- [34] Yue H, Xue LZ, Chen F. Efficiently electrochemical removal of nitrite contamination with stable RuO<sub>2</sub>–TiO<sub>2</sub>/Ti electrodes. *Appl Catal B: Environ* 2017, **206**: 683–691.
- [35] Taheri-Ledari R, Valadi K, Maleki A. High-performance HTL-free perovskite solar cell: An efficient composition of ZnO NRs, RGO, and CuInS<sub>2</sub> QDs, as electron-transporting layer matrix. *Prog Photovolt: Res Appl* 2020, **28**: 956–970.
- [36] Dalal B, Sarkar B, De SK. Itinerant to localized electronic behavior in phase segregated ruthenates. *J Alloys Compd* 2016, **667**: 248–254.
- [37] Mariolacos K. The role of electronegativity in solid solution formation: An addendum. *N Jb Miner Mh* 2003, **2003**: 215–221.
- [38] Liu ZF, E L, Ya J, *et al.* Growth of ZnO nanorods by aqueous solution method with electrodeposited ZnO seed layers. *Appl Surf Sci* 2009, **255**: 6415–6420.
- [39] Alam U, Khan A, Raza W, *et al.* Highly efficient Y and V co-doped ZnO photocatalyst with enhanced dye sensitized visible light photocatalytic activity. *Catal Today* 2017, **284**: 169–178.

- [40] Gómez-Pozos H, González-Vidal JL, Torres GA, *et al.* Chromium and ruthenium-doped zinc oxide thin films for propane sensing applications. *Sensors: Basel* 2013, **13**: 3432–3444.
- [41] Khan MAM, Kumar S, Alhazaa AN, *et al.* Modifications in structural, morphological, optical and photocatalytic properties of ZnO: Mn nanoparticles by sol–gel protocol. *Mater Sci Semicond Process* 2018, **87**: 134–141.
- [42] Son HS, Choi NJ, Kim KB, *et al.* Al-doped ZnO seed layer-dependent crystallographic control of ZnO nanorods by using electrochemical deposition. *Mater Res Bull* 2016, **82**: 50–54.
- [43] Deraz NM. Effects of heat treatment on physicochemical properties of cerium based nickel system. *J Anal Appl Pyrolysis* 2012, **95**: 56–60.
- [44] Deraz NM. Effect of NiO content on structural, surface and catalytic characteristics of nano-crystalline NiO/CeO<sub>2</sub> system. *Ceram Int* 2012, **38**: 747–753.
- [45] Chan HYH, Takoudis CG, Weaver MJ. High-pressure oxidation of ruthenium as probed by surface-enhanced Raman and X-ray photoelectron spectroscopies. *J Catal* 1997, **172**: 336–345.
- [46] Kleiman-Shwarstein A, Laursen AB, Cavalca F, *et al.* A general route for RuO<sub>2</sub> deposition on metal oxides from RuO<sub>4</sub>. *Chem Commun: Camb* 2012, **48**: 967–969.
- [47] Wang FZ, Xu Q, Tan ZA, *et al.* Efficient polymer solar cells with a solution-processed and thermal annealing-free RuO<sub>2</sub> anode buffer layer. *J Mater Chem A* 2014, **2**: 1318–1324.
- [48] Ananth A, Dharaneedharan S, Gandhi MS, *et al.* Novel RuO<sub>2</sub> nanosheets–facile synthesis, characterization and application. *Chem Eng J* 2013, **223**: 729–736.
- [49] Cox PA, Goodenough JB, Tavener PJ, *et al.* The electronic structure of Bi<sub>2-x</sub>Gd<sub>x</sub>Ru<sub>2</sub>O<sub>7</sub> and RuO<sub>2</sub>: A study by electron spectroscopy. *J Solid State Chem* 1986, **62**: 360–370.
- [50] Kwak I, Kwon IS, Kim J, *et al.* IrO<sub>2</sub>–ZnO hybrid nanoparticles as highly efficient trifunctional electrocatalysts. *J Phys Chem C* 2017, **121**: 14899–14906.
- [51] Jing LQ, Xu ZL, Shang J, *et al.* The preparation and characterization of ZnO ultrafine particles. *Mater Sci Eng: A* 2002, **332**: 356–361.
- [52] Karamat S, Rawat RS, Tan TL, *et al.* Exciting dilute magnetic semiconductor: Copper-doped ZnO. *J Supercond Nov Magn* 2013, **26**: 187–195.
- [53] Kostova B, Konstantinov L. Factors determining optical absorption of variously doped single crystals of Bi<sub>12</sub>SiO<sub>20</sub>. *J Phys: Conf Ser* 2010, **253**: 012029.
- [54] Bendavid LI, Carter EA. First principles study of bonding, adhesion, and electronic structure at the Cu<sub>2</sub>O(111)/ZnO(10 $\bar{1}$ 0) interface. *Surf Sci* 2013, **618**: 62–71.
- [55] Shao YQ, Chen ZJ, Zhu JQ, *et al.* Relationship between electronic structures and capacitive performance of the electrode material IrO<sub>2</sub>–ZrO<sub>2</sub>. *J Am Ceram Soc* 2016, **99**: 2504–2511.
- [56] Hernández RG, Pérez WL, Rodríguez MJA. Electronic structure and magnetism in Ni<sub>0.0625</sub>Zn<sub>0.9375</sub>O: An *ab initio* study. *J Magn Magn Mater* 2009, **321**: 2547–2549.
- [57] Wu HC, Peng YC, Chen CC. Effects of Ga concentration on electronic and optical properties of Ga-doped ZnO from first principles calculations. *Opt Mater* 2013, **35**: 509–515.
- [58] Lakel S, Elhamra F, Almi K, *et al.* First-principles investigation of electronic and optical properties and thermodynamic stability of Zn<sub>1-x</sub>Be<sub>x</sub>O semiconductor alloy. *Mater Sci Semicond Process* 2015, **40**: 803–810.
- [59] Tauc J. Optical properties and electronic structure of amorphous germanium. *Physica Status Solidi* 1966, **3**: 37–46.
- [60] Liu HY, Zeng F, Lin YS, *et al.* Correlation of oxygen vacancy variations to band gap changes in epitaxial ZnO thin films. *Appl Phys Lett* 2013, **102**: 181908.
- [61] Chen ZJ, Zhu JQ, Zhang S, *et al.* Influence of the electronic structures on the heterogeneous photoelectrocatalytic performance of Ti/Ru<sub>x</sub>Sn<sub>1-x</sub>O<sub>2</sub> electrodes. *J Hazard Mater* 2017, **333**: 232–241.
- [62] Zhang X, Wang JM, Liu J, *et al.* Design and preparation of a ternary composite of graphene oxide/carbon dots/polypyrrole for supercapacitor application: Importance and unique role of carbon dots. *Carbon* 2017, **115**: 134–146.
- [63] Shao YQ, Yi ZY, He C, *et al.* Effects of annealing temperature on the structure and capacitive performance of nanoscale Ti/IrO<sub>2</sub>–ZrO<sub>2</sub> electrodes. *J Am Ceram Soc* 2015, **98**: 1485–1492.
- [64] Vaiano V, Matarangolo M, Murcia JJ, *et al.* Enhanced photocatalytic removal of phenol from aqueous solutions using ZnO modified with Ag. *Appl Catal B: Environ* 2018, **225**: 197–206.
- [65] Costentin C, Drouet S, Robert M, *et al.* Turnover numbers, turnover frequencies, and overpotential in molecular catalysis of electrochemical reactions. Cyclic voltammetry and preparative-scale electrolysis. *J Am Chem Soc* 2012, **134**: 11235–11242.
- [66] Feng KK, Lin YT, Guo J, *et al.* Study on the enhanced electron-hole separation capability of Ir<sub>x</sub>Zn<sub>1-x</sub>O/Ti electrodes with high photoelectrocatalysis efficiency. *J Hazard Mater* 2020, **393**: 122488.
- [67] Mostafa AM, Menazea AA. Laser-assisted for preparation ZnO/CdO thin film prepared by pulsed laser deposition for catalytic degradation. *Radiat Phys Chem* 2020, **176**: 109020.
- [68] Beura R, Rajendran S, Gracia Pinilla MA, *et al.* Enhanced photo-induced catalytic activity of Cu ion doped ZnO–graphene ternary nanocomposite for degrading organic dyes. *J Water Process Eng* 2019, **32**: 100966.
- [69] Boudenne JL, Cerclier O, Galéa J, *et al.* Electrochemical oxidation of aqueous phenol at a carbon black slurry electrode. *Appl Catal A: Gen* 1996, **143**: 185–202.
- [70] Comninellis C. Electrocatalysis in the electrochemical conversion/combustion of organic pollutants for waste water treatment. *Electrochimica Acta* 1994, **39**: 1857–1862.
- [71] Pelegrini R, Peralta-Zamora P, de Andrade AR, *et al.*

- Electrochemically assisted photocatalytic degradation of reactive dyes. *Appl Catal B: Environ* 1999, **22**: 83–90.
- [72] Konstantinou IK, Albanis TA. TiO<sub>2</sub>-assisted photocatalytic degradation of azo dyes in aqueous solution: Kinetic and mechanistic investigations: A review. *Appl Catal B: Environ* 2004, **49**: 1–14.
- [73] Himebaugh RR, Smith MJ. Semi-micro tube method for chemical oxygen demand. *Anal Chem* 1979, **51**: 1085–1087.
- [74] Wei L, Zhu H, Mao XH, *et al.* Electrochemical oxidation process combined with UV photolysis for the mineralization of nitrophenol in saline wastewater. *Sep Purif Technol* 2011, **77**: 18–25.

**Open Access** This article is licensed under a Creative Commons

Attribution 4.0 International License, which permits use, sharing, adaptation, distribution and reproduction in any medium or format, as long as you give appropriate credit to the original author(s) and the source, provide a link to the Creative Commons licence, and indicate if changes were made.

The images or other third party material in this article are included in the article's Creative Commons licence, unless indicated otherwise in a credit line to the material. If material is not included in the article's Creative Commons licence and your intended use is not permitted by statutory regulation or exceeds the permitted use, you will need to obtain permission directly from the copyright holder.

To view a copy of this licence, visit <http://creativecommons.org/licenses/by/4.0/>.